Paper

500 kVA Medium-Frequency Core-Type Amorphous Transformers with Alternately Wound Sheet Winding for Offshore DC Grid

Naoyuki Kurita*a) Member,   Tomoyuki Hatakeyama* Member
Mamoru Kimura* Senior Member,   Kenji Nakamura** Member
Osamu Ichinokura** Senior Member

This paper describes a low winding loss design methodology to develop a real-scaled medium frequency transformer (MFT) for an isolated DC-DC converter to be used in a DC-interconnected offshore wind farm system. We assembled a core-type 500 kVA MFT consisting of a lap-joint amorphous wound core and windings with a primary Cu sheet and divided secondary Cu sheets, wound alternately in turns. Then, we compared its loss performance with that of a conventionally designed MFT. The alternately wound winding structure suppressed the medium-frequency proximity effect between the Cu sheets and the in-plane eddy current due to the fringing flux crossing the edges of the sheets and fixtures, and the winding loss at 3 kHz was 61% lower than that of the conventional MFT. In addition, we propose and discuss an accurate estimation method for the winding loss of core-type MFTs, considering the in-plane eddy current loss at the edge of the Cu sheets based on the finite element method.

Keywords: offshore wind farm, multi-winding, proximity effect, lap-joint amorphous core, leakage flux, winding loss

Nomenclature

a	Laminated thickness of amorphous core
b	Width of amorphous foil
B_m	Amplitude of magnetic flux density
B_p	Magnetic flux density component perpendicular to Cu plane
$B_{p,e}$	B_p in the endmost element of Cu sheet
C_t^A	Wound thickness of alternately wound winding
C_t^N	Wound thickness of normally wound winding
d, d', d_S	Insulation distances between Cu sheets
d_1, d_2, d_3	Insulation distances between core and winding
f	Frequency
F_R	Factor of skin and proximity effects for sheet conductors
h	Hight of primary Cu sheet
I_p, I_S	Primary and secondary currents of MFT
K	Number of modules in DC-DC converter
L	Length of Cu sheet
l_m	Mean magnetic path length of amorphous core
l_w	Mean perimeter of winding
m	Number of harmonic components
M_i	Mass of amorphous core
N	Number of turns of primary winding
n	Turn ratio of MFT
p	Number of neighboring conductor layers
P_e	In-plane eddy current loss of winding
Q	Divided number of secondary winding
R_{ac}	Combined AC resistance of winding
R_{ac1}, R_{ac2}	AC resistances of primary and secondary windings
R_{dc}	Equivalent combined DC resistance of winding
R_{dc1}, R_{dc2}	DC resistances of primary and secondary windings
S	Lamination factor of amorphous core
t	Thickness of Cu sheet
T	Period
V_{in}	Input voltage of DC-DC converter
V_{out}	Output voltage of each module in DC-DC converter
V_p, V_s	Primary and secondary voltages of MFT
V_{sys}	Output voltage of DC-DC converter
W_C	Winding loss of MFT
$W_C^{(FEM)}$	Calculated W_C with the 2D-FEM model
W_i	Core loss of MFT
W_S	Stray loss of MFT's stainless fixtures
W_t	Total loss of MFT
Δ	Ratio of thickness and skin depth of conductor
μ_s	Permeability of stainless steel
ρ	Density of amorphous foil
σ, σ_s	Conductivity of Cu and stainless steel

a) Correspondence to: Naoyuki Kurita. E-mail: naoyuki.kurita.sf @hitachi.com
* Research & Development Group, Hitachi, Ltd.
  7-2-1, Omika-cho, Hitachi, Ibaraki 319-1292, Japan
** Graduate school of Engineering, Tohoku University
  Aramaki, Aoba-ku, Sendai-shi, Miyagi 980-8579, Japan

1. Introduction

Demand for wind power systems as one of renewable energy sources to enable better environmental protection are growing [1]. Plans are being made around the world for

constructing hundreds of mega-watts classed offshore wind farms that would consist of dozens of wind turbine towers [2][3]. These offshore wind farms will be equipped with High Voltage Direct Current power transmission systems for reduction of the transmission losses. The DC-interconnected wind farm systems can be realized with an "isolated DC-DC converter" consisting of AC-DC conversion circuits and a transformer [4][5]. Moreover, a Medium Frequency Transformer (MFT) excited in the multi-kHz range enables miniatualization of the DC-DC converter [6][7].

Substantially smaller medium-frequency-excited cores would enable the design of high power density MFTs; it would also increase the loss density simultaneously. Over MW-class MFTs have used generic silicon steel or amorphous cores [8][9], while work on developing MFTs with nanocrystalline cores has also increased. So far, design methodologies considering loss, insulation, and thermal control have been developed for MFTs with operating frequencies of over 5 kHz [6][10], and performance tests have been conducted on prototypes for implementation in several applications [11][12]. Although the use of core materials with lower losses is an important way of improving the performance of high power density MFTs, the reduction of winding loss at medium frequencies remains a challenging issue.

Medium-frequency AC flows in the windings of the MFT, and the increase in AC resistance due to the skin effect in the wires and the proximity effect between neighboring wires should be considered [13]. One way to prevent this problem is to use thin wire like Litz wire. However, while optimized design methods have been studied for MFTs with thin-wire windings [14][15], MFTs for offshore wind farm systems must have a rated current on the order of several hundred amperes; a large number of thin wires need to be bundled together with a small space factor. This solution thus has problems in terms of manufacturability and the large wound thickness of the windings. Another solution is utilizing an alternately wound arrangement of primary and secondary sheet conductors, which counteracts the leakage magnetic field around the windings and reduces the AC resistance [16]. Here, schemes for designing windings for medium-frequency applications that utilize analytical methods [17]–[19] and MFT prototypes [20] have been reported. Most of the previous studies have taken the "shell-type" MFTs as the subjects of their investigations. The sheet conductors of shell-type MFT's windings are surrounded with a core, and the magnetic field vector in the core window only has a component parallel to the sheet planes. The fringing field, *i.e.*, the component perpendicular to the sheet plane, at the edges of the sheets is small, and the AC resistance of the windings can be estimated accurately [21].

We focused on the "core-type" MFT with alternately wound sheet windings. Currently, core-type transformers have been commercialized for utility-frequency applications, and low-cost manufacturing technology is available for them [22]. Most parts of the conductors in this configuration are outside of the core. The magnetic field has a large component perpendicular to the sheet plane and induces the in-plane eddy current loss; the conventional estimation method for winding loss excluding this effect is not expected to work for the windings in the core-type MFTs.

Our group demonstrated the reduction of proximity effect in the alternately wound windings of a small sized core-type test MFT and proposed a basic structure of MW-class MFT for DC-DC converter [23]. In the consideration of these results, this study demonstrated the effectiveness of a real-scaled core-type 500 kVA MFT consisting of alternately wound sheet windings and an amorphous wound core. Furthermore, we proposed an accurate estimation method for calculating winding loss of the prototyped MFT considering the in-plane eddy current loss at the edge of Cu sheets utilizing a calculable scaled three-dimensional finite element method (FEM) model.

Section 2 of this paper presents the architecture of an isolated DC-DC converter and MFT. Section 3 describes the outline of design and structure of the prototyped MFTs, while Section 4 describes the evaluation method and performance of the MFTs. Section 5 describes the aforementioned method for winding loss-estimation considering the in-plane eddy current loss on the basis of measured and analyzed results. Section 6 concludes the paper.

2. Outline of Proposed DC-Interconnected Offshore Wind Farm

Figure 1 shows the circuit diagram of the proposed DC-DC converter to be installed in the 5-MW-classed wind turbine towers of the wind farm system with DC collection and transmission capabilities. The generated AC power from a permanent magnet synchronous generator (PMSG) is converted into a DC power by a power conditioning subsystem (PCS). The converter is connected to isolated unit modules whose input and output ports in parallel and cascade, respectively [24][25]. The output voltage of the converter, V_{sys}, is defined as $K \times V_{out}$ with K being the number of modules and V_{out} being the output voltage of each module. Each unit module has an IGBT inverter and a diode rectifier on the input and output sides, respectively, and both circuits are connected through a single-phase MFT with a turn ratio of n functioning both as boost and insulation between them. Here, an insulation level on the order of several ten to hundred kilovolts is required between primary and secondary windings of MFT in the topmost module.

We propose a 3 kHz excited core-type MFT with multi-secondary windings divided in Q in consideration of conversion efficiency and the cost of the DC-DC converter that uses commercially available IGBTs and diode devices. To generate the same value of V_{out} ($= V_{in} \times n \times Q$), a higher Q
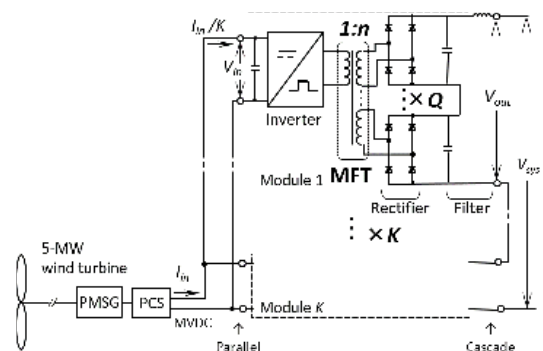

Fig. 1. Circuit diagram of the proposed isolated DC-DC converter

lowers the applied voltage in the rectifier's diodes compared with a case of $Q = 1$, which boosts only with the turn ratio, n, of the MFT. Therefore, the proposed configuration eliminates the need for the high-withstand voltage and large-loss diodes. Although the same advantage can be obtained by decreasing the capacity of the individual modules, such a configuration results in an increase in K, *i.e.*, the number of MFT units. Thus, by comparison, the proposed configuration decreases the conversion loss of the rectifiers and K simultaneously. It reduces the weight, volume, and cost of the converter.

3. 500 kVA MFTs for Functional Test

3.1 Outline of the Design This section describes the outline of the core-type MFTs using amorphous wound cores designed to test the system's effectiveness and to demonstrate the loss-reduction effect of the alternately wound winding structure. Table 1 lists the principal specifications of the prototype MFTs. For a quantitative comparison of the AC winding loss, we simultaneously assembled an MFT with the normally configured windings with primary and secondary sheets wound continuously inside and outside, respectively. The two MFTs were designed with the same conditions of cross-sectional area of core, number of turns of windings, current densities, and insulation level conformed to the DC-DC converter shown in Fig. 1.

Figures 2(a) and (b) show the cross-sectional views of the overall and winding's sheet arrangements of the prototype MFTs with two different winding structures. The external dimensions of the cores and windings were designed to ensure the margin-included insulation distances, d_1, d_2, and d_3, between the cores and windings for evaluations in air. The actual MFT is immersed in an insulation oil tank, and the winding conductor is covered with craft paper. No isolation standards have been set for large-capacity MFTs, so we chose the AC insulation level of 100 kV for a utility-frequency transformer [26]. The physical distance between the primary and secondary conductors in the alternately wound windings, d (= 5 mm), was set to ensure the above insulation level supposing the use of oil-immersed paper.

The cores for the MFTs were made of field-annealed Metglas® 2605HB1M amorphous 25 µm-thick foils [27]. A schematic manufacturing flow is shown in Fig. 3. First, cut and laminated amorphous foils are inserted in windings as shown in Fig. 3(a). Then, both ends of foils are laced in terms of 20 foils. As shown in Fig. 3(b), the wound shape of the single-phase two-legs core incorporating the two windings is formed using the lap-joint technique.

The wound thickness of alternately wound windings, C_t^A, is more than twice that of normally wound ones, C_t^N, because d against the insulation level of 100 kV is included for every turn. In contrast, the sheet-interval in C_t^N requires only d_S (= 1 mm) in the primary and secondary windings instead of using d' (= 20 mm) between them. The respective wound thicknesses can be described as follows using the parameters in Fig. 2:

Table 1. Principal specifications of the prototype 500 kVA core-type MFTs for the functional test

Configuration of windings	Alternately wound	Normally wound
Rated capacity	500 kVA	
Excitation wave	3 kHz, square	
Primary voltage, V_p / current, I_p	2.4 kV / 208 A_{rms}	
Secondary voltage, V_S / current, I_S	4.8 kV / 104 A_{rms}	
Section size of primary ($t \times h$)	0.50 mm × 200 mm	
Primary turns, N	30	30
Turn ratio, n	2	2
Division number of secondary, Q	2	1
Core material	2605HB1M amorphous	
Magnetic flux density, B_m	0.40 T	
Unit weight	595 kg	365 kg

(a) Insertion of laminated foils (b) Lacing of lap-joint part
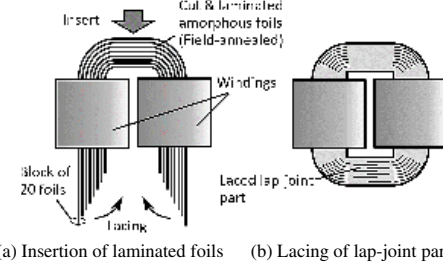
Fig. 3. Schematic manufacturing flow of a lap-joint amorphous wound core

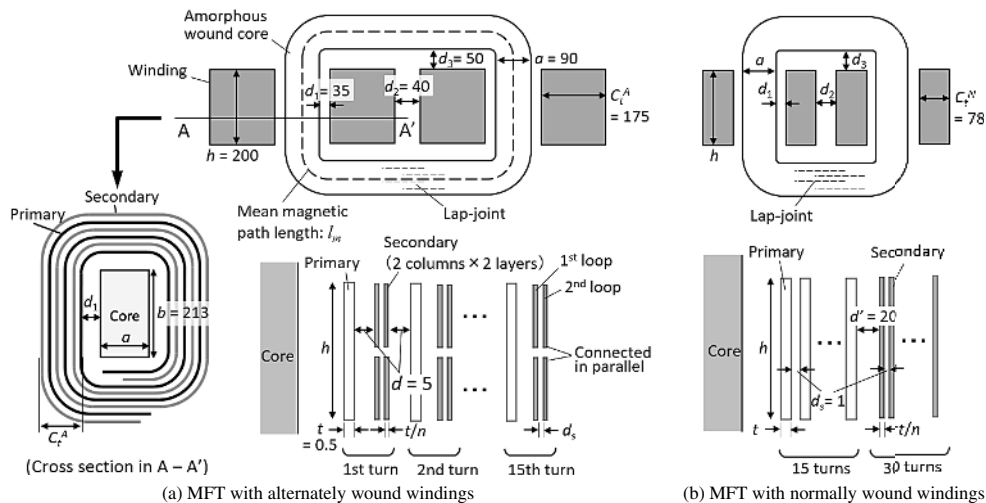(a) MFT with alternately wound windings (b) MFT with normally wound windings

Fig. 2. Cross-sectional dimension views of overall and winding's sheet arrangements of the prototype 500 kVA MFTs (Unit: mm)

$$C_t^A = \{2t + (n-1)d_s + d\}\frac{N}{2} + d\left(\frac{N}{2} - 1\right) \cdots\cdots (1)$$

$$C_t^N = Nt + \left(\frac{N}{2} - 1\right)d_s + \left(\frac{nN}{2} - 1\right)d_s + d' \cdots (2)$$

Along with this, a core for alternately wound windings is heavier than one for normally wound windings because the length of the yokes of the core is extended. The mass of the core, M_i, can be calculated by multiplying the mean magnetic path length of the core, l_m, with the effective cross-sectional area of the core and the density of the amorphous foil, ρ, as follows:

$$M_i = l_m\, a\, b\, S\, \rho \cdots\cdots\cdots\cdots\cdots\cdots\cdots\cdots (3)$$

$$l_m = 2\{2(C_t + d_1) + d_2 + h + 2d_3\} + a\pi, \cdots\cdots\cdots (4)$$

where C_t indicates C_t^A or C_t^N in response to the winding structure and $S\ (= 0.88)$ denotes the lamination factor of the core.

The alternately wound MFT has more core loss, W_i, compared with that of the normally wound one because both the MFTs have been designed for the same magnetic flux density, B_m, of 0.4 T. The iron loss per unit mass is described as a function of B_m, therefore, W_i is approximately proportional to the core's mass. In contrast, it is predicted that the winding loss, W_C, of the MFT with normally wound windings increases due to the proximity effect at medium frequencies. Additionally, for the verification of manufacturability of alternately wound and multiply divided structure of the windings and for the future studies, secondary Cu sheets were aligned in 2 columns × 2 layers ($Q = n = 2$) as the most fundamental configuration. This paper reports evaluated W_C for the case of $n = 2$ and $Q = 1$, *i.e.*, connecting the divided secondary sheets in parallel.

Photographs of the exterior of 500 kVA MFTs with alternately and normally wound windings are shown in Figs. 4(a) and (b), respectively. The upper and lower surfaces of the windings were molded with resin to secure the withstand voltage in air. Furthermore, non-magnetic stainless steel was used for the fixtures to suppress stray loss due to leakage flux

(a) MFT with alternately wound windings

(b) MFT with normally wound windings

Fig. 4. Photographs of the exteriors of the prototype 500 kVA MFTs

mainly from the windings.

3.2 Design of MFT with Alternately Wound Windings

To decide the specifications of the MFT with alternately wound windings shown in Fig. 2(a), we investigated the correlation between the magnetic flux density, B_m, and the total loss of the MFT.

This study evaluated the winding loss, W_C, of MFTs by shorting the secondary windings. In this case, the influence of core's excitation can be ignored due to the extremely larger excitation inductance of the core compared with the self and mutual inductances of windings. The winding current is approximated as a triangular waveform under a condition of a square-wave primary voltage. W_C for the triangular waveform current can be calculated as a sum of the odd modes of the harmonic components in the sinusoidal currents. From the effective value of the primary current of the fundamental ($= 3$ kHz) component, I_p, and the combined sinusoidal AC resistance measured from the primary ports at f, $R_{ac}\ (f)$, W_C can be described as

$$W_C = \sum_{k=1}^{m}\left(\frac{I_p}{2k-1}\right)^2 \cdot R_{ac}((2k-1)f). \cdots\cdots\cdots (5)$$

This study considered harmonic components, m, up to 17 ($f = 99$ kHz). R_{ac} can be described with AC resistances of primary and secondary windings, R_{ac1} and R_{ac2}, respectively, as follows:

$$R_{ac} = R_{ac1} + (1/n)^2 R_{ac2}. \cdots\cdots\cdots\cdots\cdots\cdots (6)$$

Here, R_{ac1} can be calculated as

$$R_{ac1} = F_R N l_w / (\sigma t h) \cdots\cdots\cdots\cdots\cdots\cdots\cdots (7)$$

$$l_w = 2(a + b) + (C_t^A + 2d_1)\pi, \cdots\cdots\cdots\cdots (8)$$

where σ and l_w denote the conductivity of the winding conductor and the mean perimeter of the winding, respectively. F_R, the factor of skin and proximity effects for sheet conductors and sinusoidal current, is [16]

$$F_R = \Delta\left[\frac{\sinh 2\Delta + \sin 2\Delta}{\cosh 2\Delta - \cos 2\Delta} + \frac{2(p^2 - 1)}{3} \cdot \frac{\sinh \Delta - \sin \Delta}{\cosh \Delta + \cos \Delta}\right],$$
$$\cdots\cdots\cdots\cdots\cdots (9)$$

where Δ is the ratio of the thickness of the conductor, t, and the skin depth at the operating frequency. p denotes the number of neighboring conductor layers with current in the same direction. We defined $p = 1$ for the alternately wound primary windings. R_{ac2} can be calculated in a similar way by replacing N with nN, and t with t/n, and putting $p = 2$ in equations from (7) to (9).

In this investigation, the core loss, W_i, was calculated from the previous results of excitation tests on an amorphous cut core [28]. From the faraday's law, B_m of core excited with a square voltage wave, $V(t)$, with frequency of f and height of V_p, which is defined as a quarter of the time integration of excited voltage for a period, T,

$$B_m = \frac{1}{4NabS}\int_0^T |V(t)|dt = \frac{V_p}{4NabSf}. \cdots\cdots\cdots (10)$$

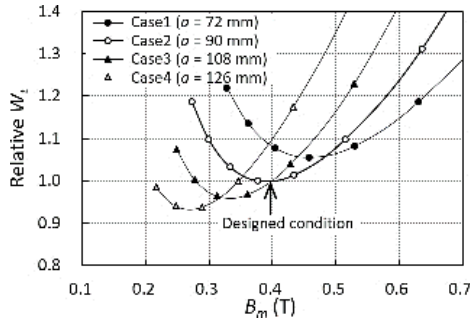W_i was calculated with a following experimental equation [28]:

Fig. 5. Calculated relative total loss, W_t, of the MFT with alternately wound windings for four cases of lamination thickness, a, of the amorphous core

$$W_i\,[W] = M_i[kg] \times (6.90 \times 10^{-3}B_m^{1.75}f$$
$$+ 9.30 \times 10^{-7}B_m^2f^2 + 2.37 \times 10^{-5}B_m^{1.5}f^{1.5})$$
$$(B_m \text{ in T}, f \text{ in Hz}).\cdots\cdots(11)$$

Figure 5 shows the B_m performances of calculated relative total loss of the MFT, W_t $(= W_i + W_C)$, in four cases of lamination thickness, a, of the core. We designed the cores with constant b $(= 213\,\text{mm})$, the as-purchased widths of the foil. Under the condition of a fixed cross-sectional area of the core, N changes in response to B_m. W_i increases as B_m increases, while W_C increases as B_m decreases because of the increase in N from the relationship in Eq. (10). Therefore, B_m with the minimum W_t could be obtained in each case. We can decide from the figure on a design for the MFT that meets the required specifications. In this study, we selected a minimum W_t condition in case 2 $(a = 90\,\text{mm})$ with $B_m = 0.40\,\text{T}$, as indicated by an arrow, considering the permissive temperature rise of core passively cooled with insulation oil [29].

4. Loss Performance of the MFT

4.1 Method of Evaluating Winding Loss, $\mathbf{W}_C$

W_C of the prototype MFTs with the secondary ports shorted was evaluated at room temperature by applying current up to 210 A_{rms} to the primary windings by using a self-assembled full-bridge inverter system consisting of two dual IGBT modules (Infineon® FF450R12ME4). A schematic of the evaluation system is shown in Fig. 6. W_C values obtained in this way include loss from the mutual resistance due to the field interaction between the primary and secondary windings. We estimated the equivalent W_C under the operating current condition of the MFTs. Square-wave voltages and triangle-waveform currents between input ports were recorded with a digital oscilloscope (LeCroy® WR HRO66i) with 12-bit resolution in the vertical direction and a bandwidth of 400 MHz. We used a differential voltage probe (Tektronix® P5200A) and a Rogowski coil (Pearson™ Model 101) for voltage and current measurements respectively. The response performance of the Rogowski coil enabled the phase shift error within 0.02% at the measured frequencies. W_C was estimated by calculating the time integral of $V\,(t) \times I\,(t)$ for a period, T,

$$W_C = \frac{1}{T}\int_0^T V(t)\cdot I(t)dt.\cdots\cdots\cdots\cdots(12)$$

4.2 Method of Evaluating Iron Loss, $\mathbf{W}_i$

Separately from W_C-evaluation, we measured core loss, W_i, of the prototype MFTs at room temperature by applying square-wave
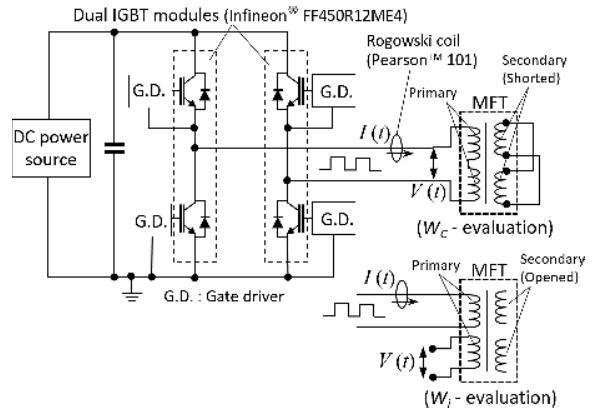

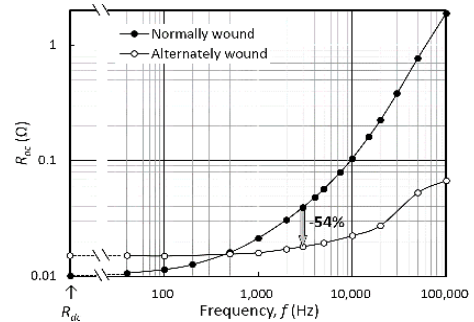Fig. 6. Schematic diagram of the measurement system for MFT's loss performance

Fig. 7. Combined sinusoidal AC resistance, R_{ac}, of the prototype MFTs as a function of frequency

voltages to the ports of the primary windings when all ports of the secondary windings were opened. As shown in Fig. 6, the primary windings in two legs were used as excitation and search coils respectively to remove the influence of winding's losses. The voltage induced in the search coil and current flowing in the excitation coil were recorded using a digital oscilloscope. The voltage probe has a large impedance of 10 MΩ; it is assumed that the influence of winding's resistance due to the skin and proximity effects can be ignored. W_i was estimated by calculating the time integral of $V\,(t) \times I\,(t)$ for a period in the same way as Eq. (12). The measured W_i is indicated in Section 4.4 for comparison of the total losses of MFTs.

4.3 Performance of Winding Loss, $\mathbf{W}_C$

Figure 7 shows the frequency performance of combined AC resistance, R_{ac}, of the windings of the prototype MFTs, measured with an LCR meter applying a sinusoidal current to the primary ports with a constant effective value of 50 mA by shorting the secondary windings. The black and white circles correspond to the measured values of the MFTs with normally and alternately wound windings. The figure includes the equivalent combined DC resistance, R_{dc}, calculated from the measured primary and secondary DC resistances, R_{dc1} and R_{dc2}, respectively, using the four-terminal method as follows:

$$R_{dc} = R_{dc1} + (1/n)^2R_{dc2}\cdots\cdots\cdots\cdots\cdots(13)$$

R_{dc} of the alternately wound winding is approximately 50% larger than that of the normally wound winding due to the difference in the wound lengths of the Cu sheets. Due

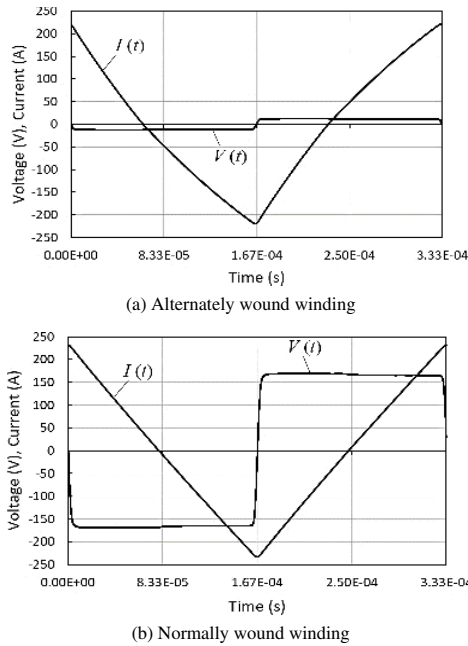(a) Alternately wound winding

(b) Normally wound winding

Fig. 8. Waveforms of primary voltage and current of the prototype MFTs with alternately and normally wound windings at $f = 3$ kHz and primary effective current of 135 A$_{rms}$
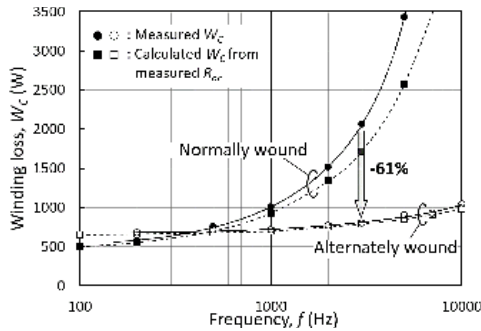

Fig. 9. Frequency performance of winding loss, W_C, of the prototype MFTs at rated current

to the proximity and skin effects, R_{ac} of the normally wound winding exceeded that of the alternately wound winding at higher than 500 Hz and reached approximately four times R_{dc} at rated frequency of 3 kHz. However, R_{ac} of the alternately wound winding increased slightly, and the value at 3 kHz was 54% lower than that of the conventional structure.

Figure 8 shows examples of the voltage and current waveforms of the primary windings when the secondary windings were shorted, and a square-wave voltage was applied to the primary ports with the IGBT inverter. The figure indicates the case of a primary effective current of 135 A$_{rms}$, equivalent to 65% of the rated current. Difference in height of primary voltage between the two MFTs is caused from the difference in leakage inductance due to the winding structures. According to the measured results with an LCR meter, the leakage inductance of the alternately wound windings was 6 to 7% of that of the normally wound ones. The alternately wound structure could suppress the leakage field effectively.

Figure 9 compares the frequency performances of rated W_C of the MFTs. The black and white circles correspond to the measured values of the MFTs with normally and
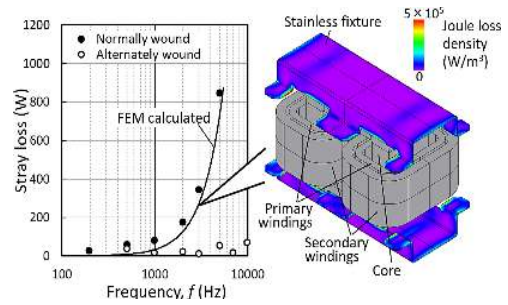

Fig. 10. (Left) Comparison of frequency performance of stray loss of MFTs, and (Right) FEM calculated contour of joule loss density in fixtures of the MFT with normally wound windings at $f = 3$ kHz

alternately wound windings. In comparison with the conventional winding, the alternately arranged structure reduced the rated W_C by 61% at 3 kHz. The black and white squares in the figure are W_C values calculated with Eq. (5) using the measured R_{ac} in Fig. 7 considering the harmonic components up to 99 kHz. The measured W_C of the normally wound winding was 17% larger than the calculated one at $f = 3$ kHz. It is conceivable that the increase in W_C was from the stray loss induced mainly at the stainless fixtures due to the crossing leakage flux. In contrast, the measured W_C of the alternately wound winding was in close agreement with the calculated values because the sheet arrangement suppressed the leakage flux.

Figure 10 compares the stray loss of the MFTs as a function of frequency. Symbols denote the numerical differences between measured and calculated W_C shown as circles and squares in Fig. 9, respectively. The figure also indicates the finite-element method (FEM) calculated stray loss on a three-dimensional (3D) model of MFT with the normally wound windings as a solid curve considering the harmonic components. On the right side of the figure, we displayed an example of joule loss (stray loss) density contour in the stainless fixtures of the MFT at $f = 3$ kHz. The contour was obtained from an electromagnetic analysis on the model with divided elements considering the skin depth at excited frequencies. The primary winding was excited by sinusoidal rated currents, and the secondary winding was shorted. The windings were approximated as bodies including respective turns of Cu sheets in which the currents flow in the same directions. In addition, the approximation cannot be applied on the alternately wound windings because the currents in neighboring Cu sheets flow in opposite directions to each other.

According to Maxwell equations, the steady state magnetic field problem can be described as

$$\text{rot}\left(\frac{1}{\mu_s}\text{rot } \boldsymbol{A}\right) = \boldsymbol{J}_s - \sigma_s\frac{\partial \boldsymbol{A}}{\partial t}, \cdots\cdots\cdots\cdots\cdots\cdots (14)$$

where μ_s and σ_s are permeability and conductivity of stainless steel, respectively, $\boldsymbol{A}$ is magnetic vector potential, $\boldsymbol{J}_s$ is current density vector. The time-averaged eddy current loss (stray loss, W_S) in stainless fixtures can be calculated with a following equation:

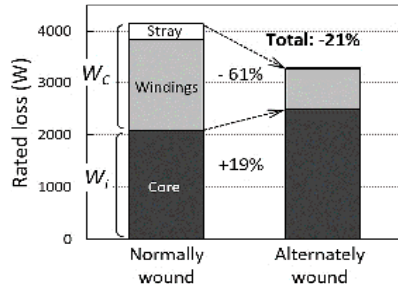$$W_S = \sum_{i=1}^{N_e} \frac{\langle \boldsymbol{J}_s^{(i)}\rangle^2}{\sigma_s}V_e^{(i)}, \cdots\cdots\cdots\cdots\cdots\cdots\cdots\cdots (15)$$

Fig. 11. Breakdown of measured rated power losses of the prototype 500 kVA MFTs at $f = 3$ kHz

(a) Normally wound windings　(b) Alternately wound windings

Fig. 12. 2D-FEM calculated contours of magnetic field distributions at the windings of the prototype 500 kVA MFTs at $f = 3$ kHz

Fig. 13. Measured and analyzed frequency performances of W_C of 500 kVA MFTs. Symbols denote the calculated W_C from measured R_{ac} in Fig. 9, while broken curves indicate the results of a 2D-FEM analysis

where N_e is number of finite element units in stainless fixtures, $V_e^{(i)}$ is volume of i-th element, brackets denote the root-mean-square of J_s in i-th element.

The calculated stray loss reasonably agrees with symbols of the MFT with normally wound windings. Therefore, it's assumed that the deviation between measured and calculated W_C in Fig. 9 is mainly due to the stray loss induced at the stainless fixtures.

The aforementioned results led us to consider that the increase in W_C of the conventionally configured core-type MFT was caused by not only the proximity and skin effects detected by the R_{ac} measurements when applying smaller current, but also the stray loss induced by the leakage flux derived from the windings. The alternating arrangement of the primary and secondary winding sheets hence effectively suppressed W_C at medium frequencies.
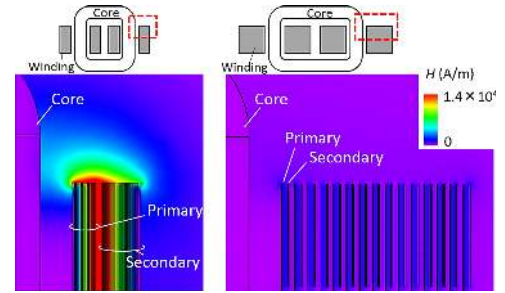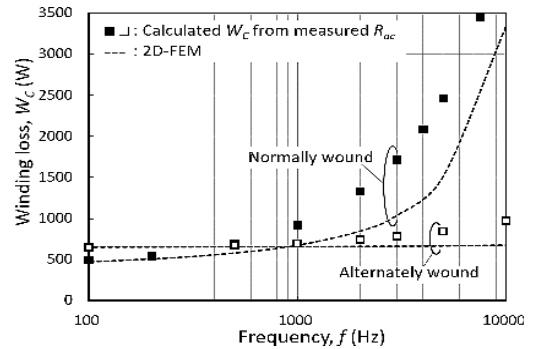
4.4 Comparison of Total Loss of MFTs Figure 11 shows breakdowns of the measured rated power losses of the two 500 kVA MFTs at $f = 3$ kHz on the basis of the W_i in the open-circuit tests and the equivalent W_C in the short-circuit tests. The figure indicates the stray loss as the difference between the measured and calculated W_C's shown in Fig. 9. The core weight of an MFT with alternately wound windings is heavier than that with normally wound windings, and the former has a 19% larger W_i (= 2487 W) than the latter (= 2082 W). Also, as described in Section 4.3, the rated W_C of the former (= 801 W) is 61% lower than that of the latter (= 2061 W). As a result, the total rated power loss of the MFT with the alternately wound windings is reduced by 21%.

5. W_C Model for Core-Type MFT

5.1 Estimation of W_C with 2D-model Figures 12(a) and (b) show the contour diagrams of the magnetic field distributions around the upper edge of the windings of the 500 kVA MFTs at $f = 3$ kHz. These results were obtained from an electromagnetic analysis using the two-dimensional FEM (2D-FEM) on longitudinal sections of individual MFT models reproduced the sheet arrangement in windings. For these calculations, the primary windings were excited by sinusoidal rated currents, and the secondary windings were shorted in the same way as in the W_C evaluations. The resistivity of the windings was 1.67×10^{-8} Ω m, supposing Cu, and the magnetization curve of the amorphous cores was defined as polynomial in a literature [23]. The case of the normally wound windings in (a) shows a large leakage field over 1.4×10^4 A/m between the primary and secondary windings. In contrast, the leakage of the alternately wound windings

shown in (b) was suppressed to approximately one tenth that of the normally wound windings. Figure 13 compares the measured and analyzed f performance of W_C of the 500 kVA MFTs not containing the stray loss. The symbols denote the W_C calculated from the measured R_{ac} as with the squares in Fig. 9. The broken curves in Fig. 13 indicate the results of the 2D-FEM analysis considering the harmonic components; they did not reproduce the values indicated with symbols. A probable cause is the effect of the fringing field. The magnetic flux density component perpendicular to the plane of the Cu sheet, B_p, is induced near the edge of windings in the core-type MFT and causes the in-plane eddy current loss, P_e, which has not been considered in the analysis. A literature [30] has revealed an underestimation of the calculated R_{ac} with 2D-FEM in the MFT's winding opened outside of the core that is similar to our results.

Figure 14 shows $B_{p,e}$, equivalent to B_p in the endmost conductor's elements, as a function of distance, x, from an innermost conductor at 3 kHz-sinusoidal rated currents. $B_{p,e}$ for the normally wound winding (the black circles) varies more with x, while those of the primary and secondary windings have maximums in the inside and outside parts, respectively. In contrast, $B_{p,e}$ for the alternately wound winding (the white circles) was less than 0.002 T and had a gentle dependence on x. A three-dimensional FEM (3D-FEM) analysis of the winding structure is needed for the calculation of P_e induced from the B_p-distribution in the edge of windings. However, 3D-FEM results in too many divided elements, which is not realistic in our situation. Hence, we attempted to estimate the P_e in the windings from the joule loss in a planar Cu sheet
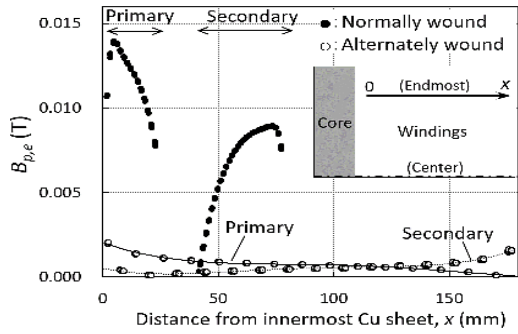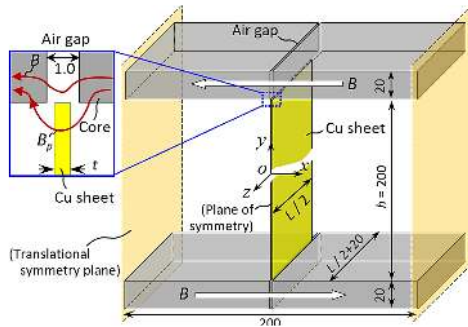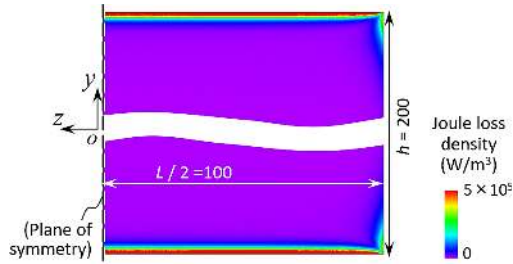
Fig. 14. Distributions of the perpendicular magnetic flux density component to the plane of Cu sheet in the endmost elements, $B_{p,e}$, in 2D-FEM as functions of the distance from innermost Cu sheet, x, at 3 kHz-sinusoidal rated currents

(a) Schematic diagram of the 3D-FEM model for P_e-estimation (Unit: mm)

(b) Contour of joule loss density in the sheet at $B_{p,e} = 0.012$ T, $f = 3$ kHz, $t = 0.5$ mm, and $L = 200$ mm

Fig. 15. Schematic diagram of the 3D-FEM model for in-plane loss, P_e-estimation in a planar Cu sheet and an example of the calculated contour of joule loss density in the sheet

made to cross B_p on a calculable scaled equivalent 3D-FEM model.

5.2 Proposal of 3D-model for In-plane Eddy Current Loss Estimation Figure 15(a) is a schematic diagram of the proposed 3D-FEM model for the P_e estimation. We made a model cut in half at the xy-plane considering symmetry, paralleled two 200-mm-long cores with rectangular cross sections with an interval of 200 mm which is the height of the winding sheet, h. The cores were defined as magnetically isotropic with the relative permeability of 1000 and electrically insulated. The translational symmetry planes were set at the both ends of the cores. The cores had the 1-mm-long air gaps and were excited in opposite x-directions to each other with the sinusoidal voltages in the coils wound around them (not shown in the figure). A planar Cu sheet 200 mm-high, t-thick and L-long was placed between the cores. The sheet corresponds to a turn of winding conductor of MFT stretched

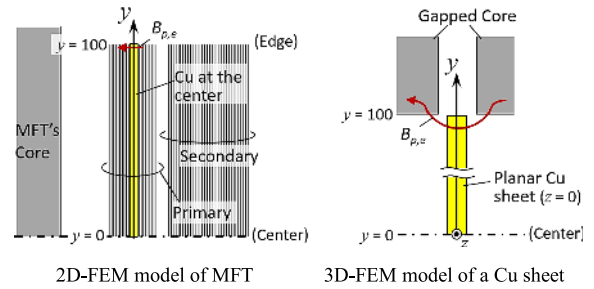2D-FEM model of MFT   3D-FEM model of a Cu sheet

Fig. 16. Calculated B_p distributions in the height (y) direction of Cu sheets at the center of primary windings in the 2D-FEM model shown in Fig. 12 (black symbols) and a planar Cu sheet in the 3D-FEM model shown in Fig. 15 (red symbols)

to the plane. As shown in the magnified inset, the arrangement enabled imitation of the B_p distribution at the edge of MFT's windings due to the fringing flux from the core gaps. By controlling of the strength of $B_{p,e}$ with the excitation voltages in the coils, the joule loss due to the in-plane eddy current, *i.e.*, P_e, in the sheet could be calculated. Figure 15(b) shows an example of the calculated contour of joule loss density in the sheet at $B_{p,e} = 0.012$ T, $f = 3$ kHz, $t = 0.5$ mm, and $L = 200$ mm; the contour shows dense loss at the upper and lower edges of the sheet.

In the proposed 3D-FEM model, the gapped cores ensured dimensions that did not affect on the B_p-distribution around a Cu sheet. The gap length of 1 mm in the cores was decided to reproduce the B_p-distribution in Cu sheets in 2D-FEM models of MFTs. Figure 16 compares examples of the calculated B_p distributions in the height (y) direction of Cu sheets at the center of primary windings in the 2D-FEM model shown in Fig. 12 and a planar Cu sheet at the plane of symmetry ($z = 0$) in the 3D-FEM model shown in Fig. 15. Schematic diagrams of the coordinate definition of Cu sheets in two models were indicated in upper part of Fig. 16. Both the distributions in normally and alternately wound windings (the black symbols) were accurately represented with the ones calculated with the 3D-FEM model (the red symbols) in accordance with the excitation voltage in the coils wound around the gapped cores.

We then surveyed the parameters of 3D-FEM model and obtained equations for P_e-estimation of primary ($t = 0.5$ mm) and secondary ($t = 0.25$ mm) sheets as functions of P_1 and P_2, respectively, for $B_{p,e}$, L, and f. Figure 17 shows examples of calculated P_1 for three cases of $B_{p,e}$ as a function of frequency at $L = 200$ mm.

From the figure, P_1 was proportional to the square of $B_{p,e}$, and it was confirmed that P_1 was proportional to L. It is
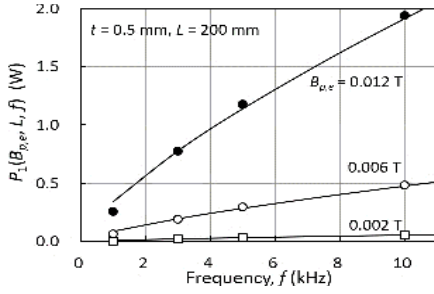
Fig. 17. Frequency performance of the in-plane eddy current loss in a planar 0.5 mm-thick Cu sheet, P_1, calculated with 3D-FEM model in Fig. 15. Symbols are calculated values, while solid curves indicate the fitted results using Eq. (16)
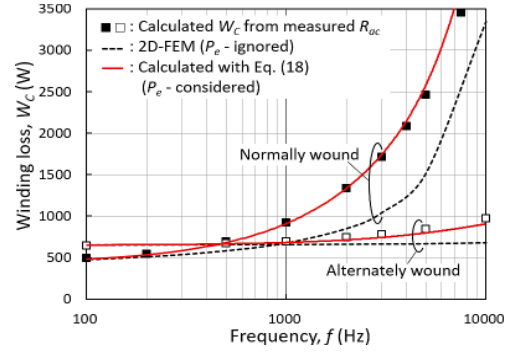
known that the growth rate of P_e in a rectangular thin conductor decreases with increase of frequency because the region where in-plane eddy current flows concentrates on the edge of conductor at higher-frequency. The analytical equation for P_e-estimation derived from Maxwell equations includes the infinite series of term consisting of the conductor's dimension and frequency [31]. Hence, we approximated P_1 in our interested frequency range with an exponential component of f. From Fig. 17, P_1 is best-fitted with 0.75 power of f and is described as

$$P_1(B_{p,e}, L, f) = A_e \cdot B_{p,e}^2 \cdot L \cdot f^{0.75}, \cdots\cdots\cdots\cdots (16)$$

where A_e is constant. Moreover, P_2 was regarded as half the P_1 because the aforementioned calculations confirmed that the eddy current loss was proportional to the thickness of Cu sheet.

P_e induced in windings at the two legs of MFT is total of P_1 and P_2 in individual turns. Therefore, P_e can be described as

$$P_e = 2 \left\{ \sum_{i=1}^{N/2} P_1(B_{p,e}^{(i)}, L^{(i)}, f) + \sum_{j=1}^{nN/2} P_2(B_{p,e}^{(j)}, L^{(j)}, f) \right\},$$
$$\cdots\cdots\cdots\cdots\cdots (17)$$

where $L^{(i)}$ and $L^{(j)}$ denote the perimeters of i-th primary and j-th secondary turns, respectively. $B_{p,e}^{(i)}$ and $B_{p,e}^{(j)}$ are found in Fig. 14.

Figure 18 compares the frequency performance of W_C in the windings in the 500 kVA MFTs between measurement and calculations. Solid red curves indicate W_C calculated with an equation below including P_e calculated with Eq. (17),

$$W_C = W_C^{(FEM)} + P_e. \cdots\cdots\cdots\cdots\cdots\cdots (18)$$

$W_C^{(FEM)}$ denotes the rated winding loss calculated from the 2D-FEM indicated by broken curves in the figure as with those in Fig. 13. Considering P_e estimated with the 3D-FEM model in Fig. 15, the calculated W_C has better agreement with that from measured R_{ac} indicated with symbols within an error of 15% at less than 5 kHz. The result in this subsection led us consider that the proposed P_e estimation method can solve a problem of underestimation of W_C with the conventional method and enables an accurate design of core-type MFT.

Fig. 18. Comparison of frequency performances of W_C of 500 kVA MFTs. Broken curves denote the results of a 2D-FEM as with Fig. 13, while solid red curves indicate the calculated results using Eq. (18) considering the in-plane loss, P_e, estimated with 3D-FEM model in Fig. 15

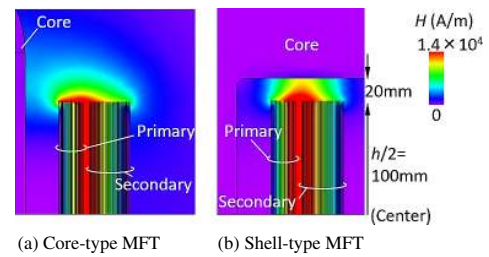(a) Core-type MFT   (b) Shell-type MFT

Fig. 19. Comparison of 2D-FEM calculated contours of magnetic field distributions at the windings of the core-type and shell-type MFTs with normally wound windings at $f = 3$ kHz

5.3 Comparison with W_C in Shell-type MFT The aforementioned discussion gives us a result that the principal cause of underestimation of the 2D-FEM calculated W_C against the measured one is due to the in-plane eddy current loss at the edge of Cu sheets outside of the core. It is predicted that B_p in the normally wound windings is reduced for a conventional shell-type MFT because the windings are surrounded with the core. An actual shell-type MFT needs a definite insulation distance between the edge of Cu sheets and core; a finite B_p induces a smaller P_e than a core-type configuration.

Figure 19 compares the contour diagrams of magnetic field distribution around the normally wound windings in core-type and shell-type MFTs with the same sheet arrangements calculated with 2D-FEM on respective longitudinal sections at 3 kHz. Figure 19(a) shows a result on the core-type MFT as with Fig. 12(a), and Fig. 19(b) denotes a result on the shell-type one with a distance of 20 mm between the edge of windings and the core as an example. It can be understood that the close core changes the field distribution of shell-type MFT from that of the core-type MFT. Figure 20 shows a comparison of $B_{p,e}$ distribution as a function of distance from an innermost Cu sheet determined in the same manner as that in Fig. 14. The $B_{p,e}$ in the shell-type MFT was decreased by approximately 40% compared with that of the core-type one. The W_C of the shell-type MFT at 3 kHz was estimated as 1130 W based on the method described in Section 5.2. In comparison with W_C's of the prototyped core-type MFTs read from black and white squares in Fig. 18, the shell-type MFT decreased W_C by 35% from that of the core-type one (=
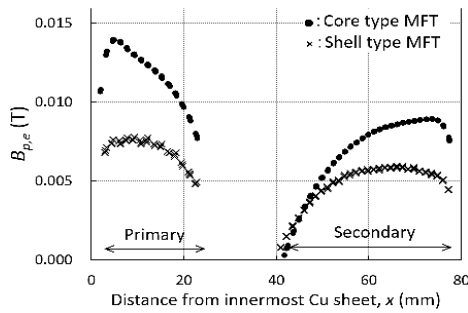
Fig. 20. Distributions of $B_{p,e}$ in 2D-FEM models of the core-type and shell-type MFTs as functions of the distance from innermost Cu sheet determined in the same manner as that in Fig. 14

1720 W) with normally wound windings. On the other hand, a core-type MFT with alternately wound windings has W_C of 790 W, 30%-smaller than W_C of the shell-type one discussed here. Consequently, the core-type MFT has the superiority in efficiency improvement by alternating the primary and secondary winding sheets.

6. Conclusion

We tested a low winding loss design of a medium frequency transformer (MFT) for an isolated DC-DC converter in a DC-interconnected offshore wind farm system. We prototyped a real-scaled core-type 500 kVA MFT consisting of a lap-joint amorphous wound core and windings with a primary Cu sheet and divided secondary Cu sheets wound alternately in turns. The windings were designed to ensure the insulation level of 100 kV between the primary and secondary sheets supposing the use of oil-immersed paper. The divided secondary windings permit a low-cost DC-DC converter with fewer modules.

The alternately wound winding structure suppresses the proximity effect between Cu sheets and the in-plane eddy current due to the fringing flux crossing the edge of sheets and fixtures, and the winding losses at 3 kHz is 61% lower than that of conventionally winding designed with the same condition of insulation level. The rated total loss of the MFT with alternately wound windings is 21% lower than that of a conventional one.

We proposed a novel estimation method for calculating winding loss of the prototyped MFT with the calculable scaled equivalent 3D-FEM model for estimation of the in-plane eddy current loss due to the fringing flux at the edge of a sheet conductor. It was verified that the frequency performance of the winding loss of the core-type MFT can be estimated within an error of 15% at less than 5 kHz.

The measured and calculated W_C of the MFTs in this study were the equivalent values when the secondary windings were shorted and a square-wave voltage was applied to the primary ports. Our future work includes evaluating the actual switching operation and the conversion efficiency of a unit module configured from an input inverter, two cascaded output rectifiers, and a prototype MFT with divided secondary windings.

Acknowledgment

References

(1) Wind Europe: "Wind energy in Europe: Scenarios for 2030", [Online]. Available: https://windeurope.org/wp-content/uploads/files/about-wind/reports/Wind-energy-in-Europe-Scenarios-for-2030.pdf
(2) J.W. Bialek: "European Offshore Power Grid Demonstration Projects", Proc. IEEE Power and Energy Soc. General Meeting, pp.1–6, San Diego, CA (2012)
(3) W. Gu: "Study on China Wind Power "Offshore Three Gorges" and Non-Grid-Connected Wind Power Industry Development", Proc. World Non-Grid-Connected Wind Power and Energy Conf. (WNWEC 2009), pp.1–4, Nanjing, China (2009)
(4) H. Liu, M. Dahidah, M. Armstrong, and R.T. Naayagi: "High Voltage High Power DC/DC Modular Multilevel Converter for Offshore Windfarm DC Collection Point", Proc. IET Inter. Conf. Power Electronics, Machines and Drives (PEMD 2016), pp.1–6, Glasgow, UK (2016)
(5) K. Musasa, N. Nwulu, M. Gitau, and R. Bansal: "Review on DC Collection Grids for Offshore Wind Farms with High-Voltage DC Transmission System", *IET Power Electronics*, Vol.10, No.15, pp.2104–2115 (2017)
(6) G. Ortiz, J. Biela, and J.W. Kolar: "Optimized Design of Medium Frequency Transformers with High Isolation Requirements", Proc. Annu. Conf. IEEE Industrial Electronics Soc. (IECON 2010), pp.631–638, Glendale, CA (2010)
(7) H. Beiranvand, E. Rokrok, B. Rezaeealam, and A. Kumar: "Optimal Design of Medium-Frequency Transformers for Solid-State Transformer Application", Proc. Inter. Power Electronics, Drive Systems and Technologies Conf. (PEDSTC 2017), pp.154–159, Mashhad, Iran (2017)
(8) N. Hugo, P. Stefanutti, and M. Pellerin: "Power Electronics Traction Transformer", Proc. European Power Electronics and Applications Conf. (EPE 2007), pp.1–10, Aalborg, Denmark (2007)
(9) S. Meier, T. Kjellqvist, S. Norrga, and H-P. Nee: "Design Considerations for Medium-Frequency Power Transformers in Offshore Wind Farms", Proc. European Power Electronics and Applications Conf. (EPE 2009), pp.1–12, Barcelona, Spain (2009)
(10) M. Amin Bahmani, T. Thiringer, A. Rabiei, and T. Abdulahovic: "Comparative Study of a Multi-MW High-Power Density DC Transformer with an Optimized High-Frequency Magnetics in All-DC Offshore Wind Farm", *IEEE Trans. Power Delivery*, Vol.31, No.2, pp.857–856 (2016)
(11) H. Hoffmann and B. Piepenbreier: "Medium Frequency Transformer in Resonant Switching dc/dc-Converters for Railway Applications", Proc. European Power Electronics and Applications Conf. (EPE 2011), pp.1–8, Birmingham, UK (2011)
(12) T.B. Gradinger, U. Drofenik, and S. Alvarez: "Novel Insulation Concept for an MV Dry-Cast Medium-Frequency Transformer", Proc. European Power Electronics and Applications Conf. (EPE 2017), pp.1–10, Warsaw, Poland (2017)
(13) P. Dowell: "Effects of Eddy Currents in Transformer Windings", Proc. Institution of Electrical Eng., Vol.113, pp.1387–1394 (1966)
(14) K.D. Hoang and J. Wang: "Design Optimization of High Frequency Transformer for Dual Active Bridge DC-DC Converter", Proc. Inter. Conf. Electrical Machines (ICEM 2012), pp.2311–2317, Marseille, France (2012)
(15) X. Liu, Y. Wang, J. Zhu, Y. Guo, G. Lei, and C. Liu: "Calculation of Core Loss and Copper Loss in Amorphous/Nanocrystalline Core-Based High-Frequency Transformer", AIP Advances, Vol.6, 055927 (2016)
(16) E.L. Barrios, A. Urtasun, A. Ursúa, L. Marroyo, and P. Sanchis: "High-Frequency Power Transformers With Foil Windings: Maximum Interleaving and Optimal Design", *IEEE Trans. Power Electronics*, Vol.30, No.10, pp.5712–5723 (2015)
(17) R. Asensi, R. Prieto, J.A. Cobos, and J. Uceda: "Modeling High-Frequency Multiwinding Magnetic Components Using Finite-Element Analysis", *IEEE Trans. Magnetics*, Vol.43, No.10, pp.3840–3850 (2007)
(18) L. Zhihua and L. Henglian: "Synthetical Analysis of Interleaving Techniques' Effect on High-frequency Transformer's Parameters", Proc. Inter. Conf. Electrical Machines and Systems (ICEMS 2008), pp.4407–4410, Wuhan, China (2008)
(19) K.V. Iyer, W.P. Robbins, and N. Mohan: "Winding Design of a High Power Medium Frequency Transformer", Proc. Inter. Sym. Power Electronics, Electrical Drives, Automation and Motion (SPEEDAM 2014), pp.665–669, Ischia, Italy (2014)

（20） M. Pavlovsky, S.W.H. de Haan, and J.A. Ferreira: "Concept of 50 kW DC/DC Converter Based on ZVS, Quasi-ZCS Topology and Integrated Thermal and Electromagnetic Design", Proc. European Power Electronics and Applications Conf. (EPE 2005), pp.1–9, Dresden, Germany (2005)

（21） M. Amin Bahmani, T. Thiringer, and H. Ortega: "An Accurate Pseudoempirical Model of Winding Loss Calculation in HF Foil and Round Conductors in Switchmode Magnetics", *IEEE Trans. Power Electronics*, Vol.29, No.8, pp.4231–4246 (2014)

（22） S. Yurekten, A. Kara, and K. Mardikyan: "Energy Efficient Green Transformer Manufacturing with Amorphous Cores", Proc. Inter. Conf. Renewable Energy Research and Applications (ICRERA 2013), pp.534–536, Madrid, Spain (2013)

（23） H. Tanaka, K. Nakamura, and O. Ichinokura: "Winding Arrangement of High-Frequency Amorphous Transformers for MW-class DC-DC Converters", *J. Magnetics Soc. Japan*, Vol.40, No.2, pp.35–38 (2016)

（24） J.F. Zhao, J.G. Jiang, and X.W. Yang: "AC-DC-DC Isolated Converter with Bidirectional Power Flow Capability", *IET Power Electronics*, Vol.3, No.4, pp.472–479 (2010)

（25） H. Krishnamoorthy, M. Daniel, J. Ramos-Ruiz, P. Enjeti, L. Liu, and E. Aeloiza: "Isolated AC-DC Converter Using Medium Frequency Transformer for Off-Shore Wind Turbine DC Collection Grid", *IEEE Trans. Industrial Electronics*, Vol.64, No.11, pp.8939–8947 (2017)

（26） International Electrotechnical Commission: "Power transformers—Part 3: Insulation levels, dielectric tests and external clearances in air", IEC 60076-3:2013 (2013)

（27） K. Takahashi, D. Azuma, and R. Hasegawa: "Acoustic and Soft Magnetic Properties in Amorphous Alloy-Based Distribution Transformer Cores", *IEEE Trans. Magnetics*, Vol.49, No.7, pp.4001–4004 (2013)

（28） N. Kurita, K. Onda, K. Nakanoue, and K. Inagaki: "Loss Estimation Method for Three-Phase AC Reactors of Two Types of Structures Using Amorphous Wound Cores in 400-kVA UPS", *IEEE Trans. Power Electronics*, Vol.29, No.7, pp.3657–3668 (2014)

（29） R.U. Lenke, S. Rohde, F. Mura, and R. De Doncker: "Characterization of Amorphous Iron Distribution Transformer Core for Use in High-Power Medium-Frequency Applications", Proc. IEEE Energy Conversion Congress and Exposition (ECCE 2009), pp.1060–1066, San Jose, CA (2009)

（30） M. Chen, M. Araghchini, K.K. Afridi, J.H. Lang, C.R. Sullivan, and D.J. Perreault: "A Systematic Approach to Modeling Impedances and Current Distribution in Planar Magnetics", Proc. IEEE Workshop on Control and Modeling for Power Electronics (COMPEL 2014), pp.1–17, Santander, Spain (2014)

（31） M. Krakowski: "Eddy-Current Losses in Thin Circular and Rectangular Plates", *Archiv für Elektrotechnik*, Vol.64, No.6, pp.307–311 (1982)

Naoyuki Kurita (Member) received the M.Eng. and Ph.D. Eng. degrees from Tohoku University, Sendai, Japan, in 1995 and 2018. From 1995 to 2010, he worked in Central Research Laboratory, Hitachi Ltd., where he was responsible for development of communication and automotive radar systems using millimeter-wave analog ICs. Since 2010, he has been engaged in research for static electromagnetic machines for power electronics and power systems at Hitachi Research Laboratory, Hitachi Ltd. Dr. Kurita is a member of The Magnetics Society of Japan.

Tomoyuki Hatakeyama (Member) received Bachelor of Engineering and Master of Information Science and Technology from Hokkaido University, Sapporo, Japan, in 2007 and 2009, respectively. Since 2009, he has been with Hitachi Research Laboratory, Hitachi Ltd., where he has engaged in research of power electronics and wind turbine systems. In 2014 and 2015, he has been with Hitachi Europe GmbH, where he conducted joint research with RWTH Aachen University, Aachen, Germany. Mr. Hatakeyama is a member of IEEE and CIGRE.

Mamoru Kimura (Senior Member) was born on July 7, 1974. He received his M.Eng. and Ph.D.Eng. degrees from Tohoku University, Sendai, Japan in 1999 and 2014. In 1999 he joined Hitachi Research Laboratory, Hitachi Ltd. Since then he has been engaged in the study of rotating machines and wind turbine systems. Dr. Kimura is a member of IEEE.

Kenji Nakamura (Member) received the B.E. and M.E. degrees from Tohoku University in 1998 and 2000. He was with Tohoku University as a Research Associate in the Graduate School of Engineering from 2000 to 2007. In 2007, he received the Ph.D. degree from Tohoku University, where he is currently a Professor of the Graduate School of Engineering. His current research interests include the design and analysis of electrical machines and their industrial applications. Prof. Nakamura is a member of The Magnetics Society of Japan, Society of Automotive Engineers of Japan, Inc. and IEEE.

Osamu Ichinokura (Senior Member) received his Ph.D. degree in Electrical Engineering from Tohoku University in 1980. From 1980 to 1988, he was a Research Assistant in the Department of Electrical Engineering of Tohoku University. From 1988 to 1995, he was an Assistant Professor in the Department of Electrical Engineering of Tohoku University. From 1995 to 2017, he was a Professor in the Department of Electrical Engineering of Tohoku University. He is currently a Professor in New Industry Creation Hatchery Center (NICHe) of Tohoku University. He is interested in power electronics and power magnetics. He is a member of The Magnetics Society of Japan and IEEE.